ROYAL SOCIETY
OF CHEMISTRY

PAPER

Check for updates

Wet-spun Ni, N-codoped macroporous carbon fibers for efficient CO_2 electroreduction and Zn–CO_2 batteries†

Liu Han,[a] Cheng-wei Wang,[a] Hai-ping Xu,[ab] Ming Yang,*[cd] Bing Li [ID] *[ab] and Ming Liu [ID] *[a]

Developing efficient and cost-effective electrocatalysts for the electrocatalytic CO_2 reduction reaction (eCO_2RR) is highly desirable for carbon neutrality and clean energy. Herein, a self-sacrificing template-assisted wet spinning method is developed to fabricate 3D interconnected Ni, N-codoped macroporous carbon fibers (Ni-NMCF), which possess a uniform distribution of Ni, a large surface area, and abundant accessible active sites. The optimized catalyst, Ni-NMCF-10, shows a high CO faradaic efficiency (FE_{CO}) over 95% in the potential range from −0.6 to −1.2 V (*vs.* RHE) and achieves a maximum FE_{CO} of 99.4% at −0.8 V (*vs.* RHE). When it is used as a cathode catalyst, the resulting Ni-NMCF-10-based Zn–CO_2 batteries present a maximum power density of 2.4 mW cm^{-2} and FE_{CO} of 98.7%.

1. Introduction

The increasing global warming and growing energy demand have sparked great interest in the reuse of the greenhouse gas CO_2 to achieve the anthropogenic carbon cycle and the use of renewable energy sources such as solar, wind and tidal energy to power human activities.[1,2] The electrocatalytic carbon dioxide reduction reaction (eCO_2RR) offers an attractive method to alleviate the greenhouse effect and achieve a carbon-neutral society.[3–5] The fundamental and practical dimensions of the eCO_2RR have garnered significant attention in recent years.[6–9] Among the reduction products, carbon monoxide (CO) stands out as a promising candidate.[10,11] It can be used as fuel in CO fuel cells and as a feedstock for synthesizing hydrocarbons *via* Fischer–Tropsch reactions.[12,13] Thus, CO both serves as an energy storage medium and has significant economic value. Nevertheless, the activation of inert CO_2 molecules requires overcoming the high reaction energy barrier, resulting in a large overpotential to achieve high product selectivity and the desired current density.[14–16] In addition, the inevitable competing hydrogen evolution reaction (HER) results in a decrease in the

selectivity of the reduction products.[17,18] Hence, developing an efficient and cost-effective electrocatalyst to reduce the activation energy barriers and inhibit the HER is urgent for the practical applications of the eCO_2RR. Among the numerous eCO_2RR catalysts reported, metal–nitrogen–carbon (M–N–C) catalysts have demonstrated significant potential for high catalytic activity and selectivity, cost-effectiveness, chemical stability, and tunable properties.[19–21] In particular, Ni–N–C materials have emerged as notable candidates for the eCO_2RR, exhibiting exceptional catalytic activity and selectivity. These properties make them promising frontrunners in advancing the development of electrocatalytic CO_2 conversion technologies.[22–24] For example, Xie and co-workers reported a Ni–N_4 structure obtained through a topochemical transformation strategy, which exhibited a FE_{CO} higher than 90.0% over a potential range from −0.5 V to −0.9 V (*vs.* reversible hydrogen electrode (RHE)).[25] Additionally, numerous studies focusing on Ni–N–C catalysts have demonstrated comparable electrocatalytic performance. Nevertheless, the primary difficulty faced by most Ni–N–C catalysts lies in their constrained operational voltage range, an essential criterion for maintaining a high selectivity towards CO.[26–28] This limitation renders them less adaptable to voltage fluctuations, particularly when intermittent renewable energy sources are used as the primary driving force in practical applications. In general, the performance of Ni–N–C materials at a low overpotential region ($\sim$−0.45 V) is weaker than that of other transition metal-based materials because it needs to overcome a higher reaction energy barrier to convert CO_2 into COOH*. Therefore, a high CO selectivity can be obtained at low overpotentials by combining Ni–N–C materials with other transition metal-based materials.[29–31] However, the CO selectivity of Ni–N–C materials

[a] School of Chemistry and Chemical Engineering, Harbin Institute of Technology, Heilongjiang, 150000, China. E-mail: bing.li2020@hit.edu.cn; liuming0117@hit.edu.cn

[b] State Key Laboratory of Space Power-Sources, School of Chemistry and Chemical Engineering, Harbin Institute of Technology, Heilongjiang, 150000, China

[c] Department of Applied Physics, The Hong Kong Polytechnic University, Hung Hom, Hong Kong SAR, China. E-mail: kevin.m.yang@polyu.edu.hk

[d] Research Centre on Data Sciences & Artificial Intelligence, The Hong Kong Polytechnic University, Hung Hom, Hong Kong SAR, China

This journal is © The Royal Society of Chemistry 2025

J. Mater. Chem. A, 2025, 13, 2707–2715 | **2707**

at high overpotentials (<−1 V) is influenced by various factors such as mass transport limitations, more intense HER, and catalyst self-reconstruction.[32–34]

So far, it is widely expected that the microstructural arrangement of the catalyst plays a vital role in determining the accessibility of active sites and facilitating the mass transport of reactants, leading to catalytic performance enhancement. As a result, the deliberate regulation of morphology or the tailored engineering of structure has emerged as a promising strategy for well-designed advanced Ni–N–C catalysts with superior performance.[35,36] To enhance the accessibility of active sites, a variety of porous carbon architectures with varying morphologies and pore size distribution have been synthesized using techniques such as the hard-template method and block copolymer self-assembly approach.[37,38] Integrating multimodal pore size distribution encompassing interconnected macro-, meso-, and micropores enables a streamlined pathway to effectively direct reactants and electrolytes toward the active sites, optimizing catalytic performance.[39,40] Nevertheless, the intricate, costly, and severe synthesis conditions are accompanied by challenges like low catalyst yield and poor repeatability. Hence, it is urgent and necessary to explore more convenient and economical techniques for the fabrication of porous Ni–N–C materials.

Herein, we develop a facile and economical self-sacrificing template-assisted wet spinning method to construct a 3D interconnected Ni, N-codoped macroporous carbon fiber (Ni-NCMF). The detailed synthesis process is shown in Fig. 1a. At room temperature, the supramolecule (MCA) sphere was prepared by a modified molecular cooperative assembly between melamine and cyanuric acid.[41,42] The as-obtained MCA spheres are well mixed with nickel acetylacetonate (Ni(acac)$_2$) and polyacrylonitrile (PAN) before being wet spun into composite fibers (Fig. S1†). This novel wet-spinning technique is capable of synthesizing a large quantity of composite fibers within a short time. By subsequent thermal annealing, the composite fibers are converted into 3D interconnected Ni-NMCF. During the pyrolysis process, the MCA sphere acts as a sacrificial template for porous structure generation and a rich nitrogen source while omitting the subsequent etching steps needed. The 3D interconnected, highly porous, and conductive structure of Ni-NMCF provides abundant accessible active sites and promotes fast electron/mass transfer properties. Consequently, the obtained Ni-NMCF catalyst exhibits high selectivity towards the eCO$_2$RR. An optimized Ni-NMCF-10 catalyst exhibited a faradaic efficiency of >95% over the potential range from −0.6 to −1.2 V for CO conversion and achieved a maximum FE$_{CO}$ of 99.4% at −0.8 V.

2. Results and discussion

2.1. Fabrication and characterization of Ni-NMCF-T

Scanning electron microscopy (SEM) (Fig. S2a and b†) images showed that the MCA spheres possess a rough surface with an average diameter of around 2–3 μm. Elemental mapping images of MCA spheres confirmed the uniform distribution of C and N elements (Fig. S2c†). Using a wet spinning technique, the precursor solution containing MCA spheres, Ni(acac)$_2$, and PAN was directly injected into deionized water and rapidly transformed into a white fiber (Fig. S3†). The MCA spheres were intricately integrated with PAN during the spinning process, and Ni(acac)$_2$ was evenly dispersed on the substrate. Subsequent annealing at the specified temperature for 2 hours in the N$_2$ atmosphere led to the complete decomposition of the MCA spheres, leaving 3D interconnected Ni, N-codoped macroporous carbon fibers (Ni-NMCF). By adjusting the amount of Ni(acac)$_2$ to 1, 10, and 100 mg while keeping the amount of MCA fixed in the precursor solutions, three catalysts with different Ni contents were obtained and labeled as Ni-NMCF-x (where x represents the feeding amount of Ni(acac)$_2$; the actual Ni amounts for the three samples are 0.13, 0.32 and 1.52 wt% determined by Inductively Coupled Plasma Optical Emission Spectroscopy (ICP-OES) analysis respectively (Table S1†)). It is worth noting that no additional nitrogen source is required during the pyrolysis process, and the obtained catalyst can be directly used for performance testing without the subsequent complex etching or re-calcination processes. This can be attributed to the complete decomposition of the supramolecular precursor during the pyrolysis process, leaving a hollow structure and providing a rich source of nitrogen. The SEM images of Ni-NMCF-10 displayed porous fiber networks with fiber diameters of 20–40 μm (Fig. S4a and b†). The high-magnification SEM images revealed that the rough surface of Ni-NMCF-10 consisted of numerous interconnected hollow hemispheres derived from the MCA sphere and PAN in a disordered distribution used as 3D carbon skeletons (Fig. 1b and c).

Transmission Electron Microscopy (TEM) images further revealed the random distribution of hollow hemispheres embedded in the carbon skeletons without obvious Ni nanoparticles (NPs) being observed (Fig. 1d). The elemental mapping analysis of Ni-NMCF-10 disclosed the presence and homogeneous distribution of C, N, O, and Ni elements (Fig. 1e). As shown in Fig. S5–S9,† all Ni-NMCF-x and Ni-NMCF-10 (T) catalysts exhibited similar features of 3D interconnected carbon macroporous fibers and homogeneously distributed C, N, and O elements. The absence of a Ni signal in the Ni-NMCF-1 suggests its very low content. Meanwhile, the control sample, Ni NPs-NCM, showed Ni nanoparticles embedded in the carbon skeleton (Fig. S10a–c†) and randomly dispersed (Fig. S10d†), suggesting that the conventional synthesis method is prone to lead to aggregation of Ni species during pyrolysis.

A broad peak at about 21.7°, corresponding to the (002) planes of graphitic carbon (Fig. 2a), was observed in the XRD patterns of NMCF, Ni-NMCF-10, and Ni NPs-NMC catalysts, indicating the successful conversion of PAN to graphitic carbon at this temperature. Meanwhile, three diffraction peaks at 44.5°, 51.7°, and 76.3°, attributed to the (111), (200), and (220) planes of metallic Ni, respectively (PDF #04-0850), were observed on the Ni NPs-NMC catalysts, demonstrating the existence of metallic Ni. The absence of obvious metallic Ni peaks in the Ni-NMCF-10 catalyst suggests the low content of Ni or that Ni exists in a monodispersed state, which agrees with the observations of TEM imaging (Fig. 1d) and elemental mapping (Fig. 1e). In addition, the characteristic peaks of Ni-NMCF obtained at
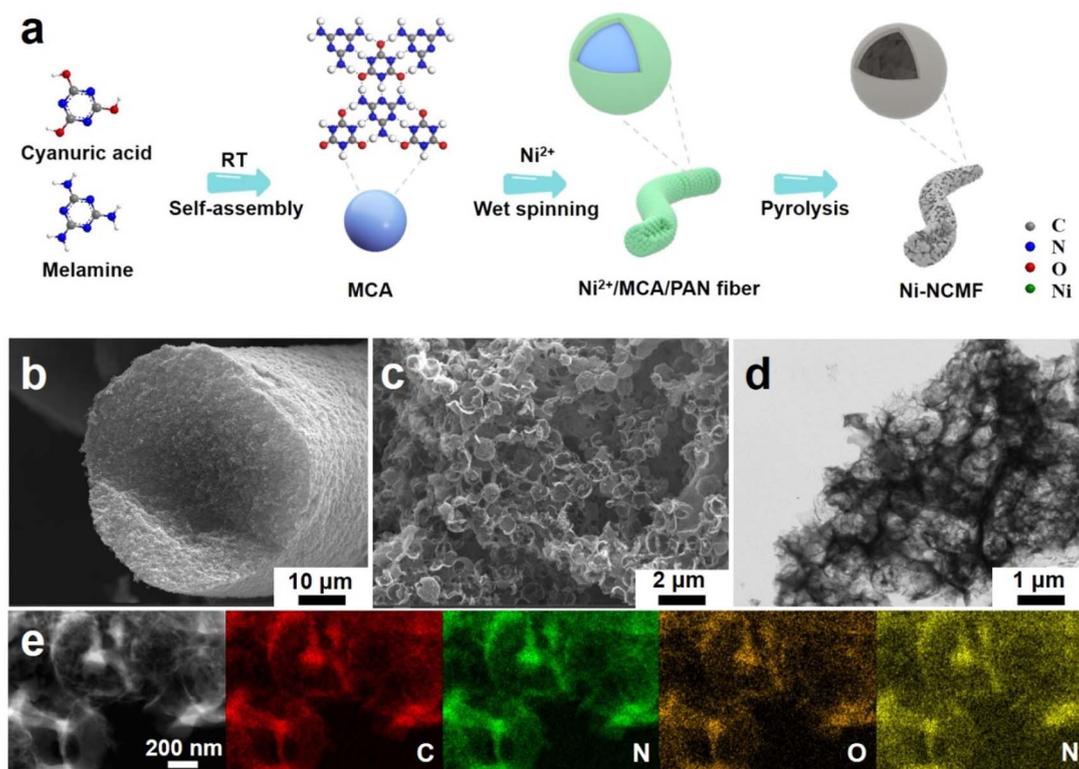
2708 | *J. Mater. Chem. A*, 2025, **13**, 2707–2715

This journal is © The Royal Society of Chemistry 2025

Fig. 1 Catalyst preparation process and morphology characterization. (a) Schematic illustration of the preparation route for Ni–NMCF. (b and c) SEM images, (d) TEM image, and (e) EDX elemental mapping of Ni–NMCF-10.

different Ni content or pyrolysis temperatures were similar to those of Ni-NMCF (Fig. S11a and b†). The specific surface areas and pore size distributions of catalysts were investigated through N_2 adsorption–desorption tests. NMCF, Ni-NMCF-10, and Ni NPs-NMC catalysts all exhibit typical hysteresis loops (Fig. S12a†), indicating the presence of abundant micropores and mesoporous structures in these catalysts. The NMCF catalyst demonstrates the largest specific surface area of 546.8 m^2 g^{-1}, surpassing that of Ni-NMCF-10-900 (452.0 m^2 g^{-1}) and Ni NPs-NMC (328.8 m^2 g^{-1}). The decrease in the specific surface area of Ni-NMCF-10-900 and Ni NPs-NMC may be attributed to additional coordination by Ni^{2+} and –NH$_2$ groups hindering the pores.[43] The pore size distribution curves further confirm the presence of numerous micropores and mesoporous structures in the catalysts (Fig. S12b†). The micropores and mesopores are most probably caused by the release of small gas molecules derived from the decomposition of the MCA precursor. Together with macropores caused by the complete decomposition of MCA precursors, all samples show a hierarchical pore structure. The larger specific surface area exposes more accessible active sites, enhancing CO_2 molecule adsorption, while the hierarchical pore distribution reduces the transfer distance of reactants, thereby promoting enhanced mass transfer.[44,45] The Raman spectra of the three catalysts exhibited two peaks at around 1359 and 1576 cm^{-1}, corresponding to disordered sp^3 carbon (D band) and graphitic sp^2 carbon (G band), respectively (Fig. 2b). It should be noted that the Ni NPs-NMC catalyst

showed the lowest I_D/I_G value (0.93), which might be attributed to the higher degree of graphitization catalyzed by the Ni NPs. In addition, the Ni content has a negligible effect on the I_D/I_G value of Ni-NMCF-x samples (Fig. S13a†). However, the I_D/I_G value decreased with the increase in pyrolysis temperature credited to the enhanced extent of graphitization and reduced nitrogen defect density (Fig. S13b†).[36,46] X-ray photoelectron spectroscopy (XPS) was carried out to study the chemical composition and elemental states of the catalyst surfaces. As shown in Fig. S14,† the high-resolution C 1s spectrum of all prepared samples displayed three deconvoluted peaks at 284.8 eV, 285.8 eV, and 288.4 eV, corresponding to C–C, C–N, and O–C–O, respectively, demonstrating the successful doping of N species in the carbon skeleton. The Ni NPs-NMC catalyst predominantly exhibits two Ni 2p$_{3/2}$ peaks at 853.3 eV and 854.5 eV, corresponding to metallic Ni^0 and Ni^{2+}, respectively.[47,48] Accordingly, the Ni 2p$_{1/2}$ can be deconvoluted into two peaks at 870.7 eV and 872.1 eV, which are attributed to Ni^0 and Ni^{2+}. In the case of the Ni-NMCF-10 catalyst, the Ni 2p$_{3/2}$ characteristic peak shifted to a higher binding energy compared to that of Ni^0 (Fig. 2c). This shift suggests the formation of Ni–N bonds and validates the low-content metallic Ni,[49] as has been observed by XRD, ICP, and TEM characterizations. In contrast, it is worth noting that the Ni content and pyrolysis temperature have no significant effect on the final valence state of the Ni-NMCF-x and Ni-NMCF-10 (T) catalysts (Fig. S15a and b†). The high-resolution N 1s spectrum could be divided into pyridinic-N

This journal is © The Royal Society of Chemistry 2025

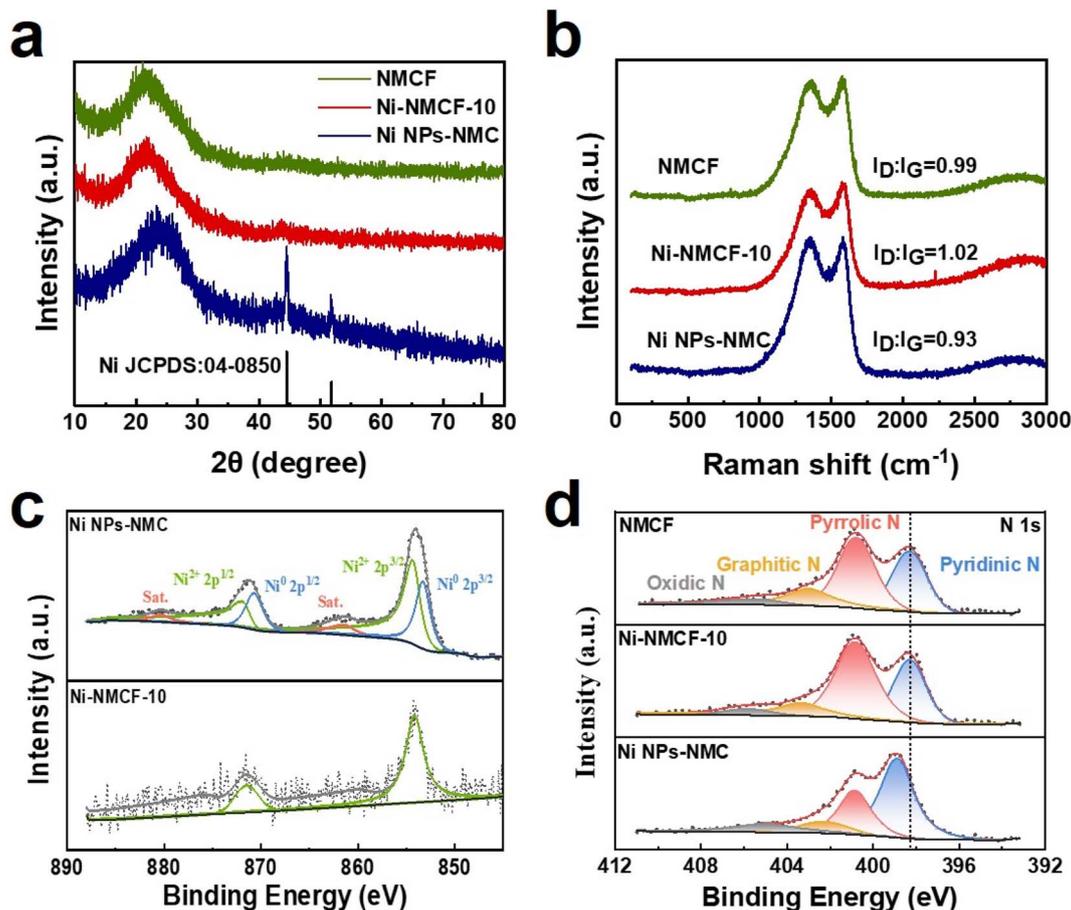J. Mater. Chem. A, 2025, 13, 2707–2715 | 2709

Fig. 2 The structure characterization of catalysts. (a) XRD patterns, (b) Raman spectra, (c) Ni 2p, and (d) N 1s XPS spectra of NMCF, Ni-NMCF-10, and Ni NPs-NMC.

($\sim$398.3 eV), pyrrolic-N ($\sim$400.8 eV), graphitic-N ($\sim$403.0 eV), and oxidized-N ($\sim$405.7 eV) (Fig. 2d). Compared to NMCF and Ni-NMCF-10, the binding energy of pyridinic N shifted to a higher value and its relative content also increased for the Ni NPs-NMC catalyst, which is probably due to the bonding of Ni species with pyridinic N.[46,50,51] In the Ni-NMCF-x catalyst, a similar trend was observed, where the binding energy of pyridinic-N increased with the increase in Ni content (Fig. S16a†). Interestingly, the relative content of pyridinic-N decreased while that of other N species remained nearly constant as the pyrolysis temperature increased (Fig. S16b†). This could be attributed to residual water molecules in the nitrogen gas during pyrolysis, which preferentially adsorb onto pyridinic-N rather than pyrrolic-N. Consequently, the carbon atoms adjacent to pyridinic-N are more easily etched, leading to a greater loss of pyridinic-N compared to pyrrolic-N.[52]

2.2. Electrocatalytic properties

Inspired by the above results, the electrochemical activity of the prepared catalysts for the eCO$_2$RR in a gas-tight H-type cell was evaluated. The LSV curves of Ni-NMCF-10 and Ni NPs-NMC showed an enhanced current density in a CO$_2$-saturated KHCO$_3$ electrolyte than in the Ar atmosphere, indicating the

considerable CO$_2$ reduction potential. In comparison, the current densities exhibited by the NMCF catalyst were similar in both CO$_2$ and Ar atmospheres, implying its inadequate performance in CO$_2$ reduction (Fig. 3a). Furthermore, the LSV curves of all Ni-NCMF-x and Ni-NCMF-10 (T) samples showed enhanced current density in the CO$_2$ atmosphere, indicating the excellent universality of our synthesis method (Fig. S17†).

Subsequently, a chronoamperometric technique was conducted at different applied potentials to evaluate the electrochemical properties of the catalyst. Gas chromatography (GC) and ^{1}H nuclear magnetic resonance (NMR) spectroscopy confirmed the gaseous products including H$_2$ and CO while no liquid product was detected (Fig. S18†). The calculated Faraday efficiency of CO (FE$_{CO}$) and the corresponding partial current densities (j_{CO}) versus different applied potentials are presented in Fig. 3b and c. The metal-free NMCF catalyst demonstrates inferior CO$_2$ reduction performance across the entire range of applied potentials, with optimal FE$_{CO}$ and j_{CO} values reaching only 65.7% and 2 mA cm^{-2}, respectively. H$_2$ was the major product for NMCF, indicating that the HER was the dominant process during the CO$_2$RR over the applied potential range (Fig. S19†). This poor CO$_2$ reduction activity can be attributed to low active sites and inadequate electrical conductivity. As
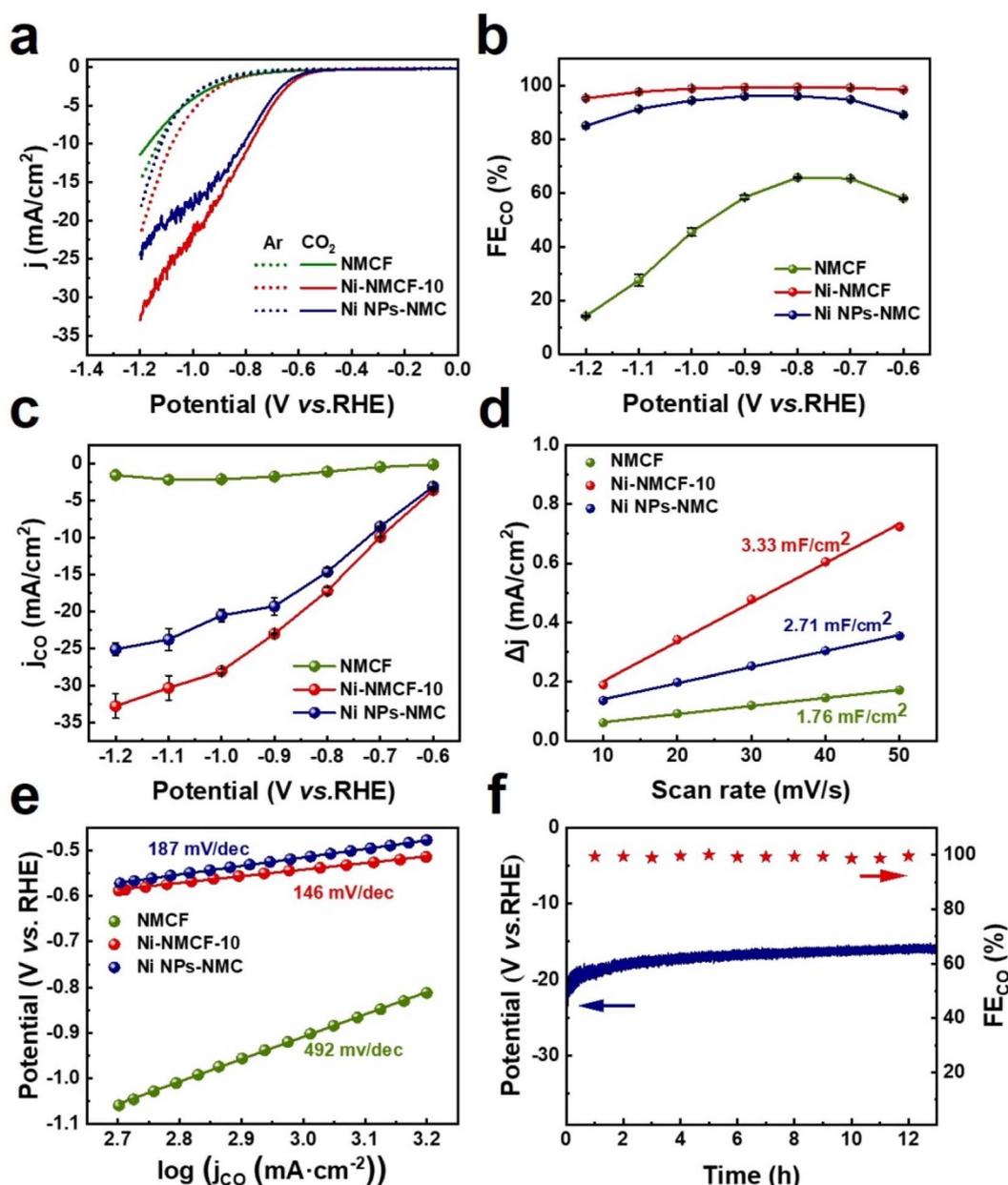
2710 | J. Mater. Chem. A, 2025, 13, 2707–2715

This journal is © The Royal Society of Chemistry 2025

Fig. 3 Electrocatalytic performance characterization: (a) LSV curves in Ar (dotted lines) and CO_2-saturated (solid lines) 0.5 M $KHCO_3$ electrolyte at a scan rate of 10 mV s^{-1} for NMCF, Ni-NMCF-10, and Ni NPs-NMC; (b) FE_{CO} and (c) j_{CO} of NMCF, Ni-NMCF-10, and Ni NPs-NMC catalysts in the H-type cell; (d) dependence of charging current density differences (Δj) *versus* scan rates and (e) Tafel plots of NMCF, Ni-NMCF-10, and Ni NPs-NMC catalysts; (f) long-term stability tests of the Ni-NMCF-10 catalyst at −0.8 V in the H-type cell.

expected, the high selectivity of the Ni-NMCF-10 catalyst reached nearly 100% towards CO. Specifically, it also showed a FE_{CO} of >95% across a broad potential window from −0.6 to −1.2 V. A maximum FE_{CO} of 99.4% was obtained at −0.8 V, which is better than most of the reported state-of-the-art Ni-based electrocatalysts under similar conditions (Fig. S20 and Table S2†).

In contrast to the notably low j_{CO} exhibited by the NMCF catalyst, the Ni-NMCF-10 catalyst also presented a large j_{CO} of 17.2 and 32.7 mA cm^{-2} at −0.8 and −1.2 V, respectively. Interestingly, the Ni NPs-NMC catalyst also demonstrated a good

CO_2 reduction performance. This further confirms the superiority of using the MCA sphere as a self-sacrificing template for catalyst preparation. However, FE_{CO} and j_{CO} were notably lower than those of the Ni-NMCF-10 catalyst throughout the entire potential range. Meanwhile, our observations show that an increase in Ni content increases j_{CO} but reduces FE_{CO} (Fig. S21a and b†). This can be explained as more Ni providing additional reaction sites for the eCO_2RR, thus leading to a higher j_{CO}. However, excessive Ni can cause aggregation, which favors the HER and in turn reduces the FE_{CO}. We also found that the pyrolysis temperature has minimal effect on the FE_{CO}, although
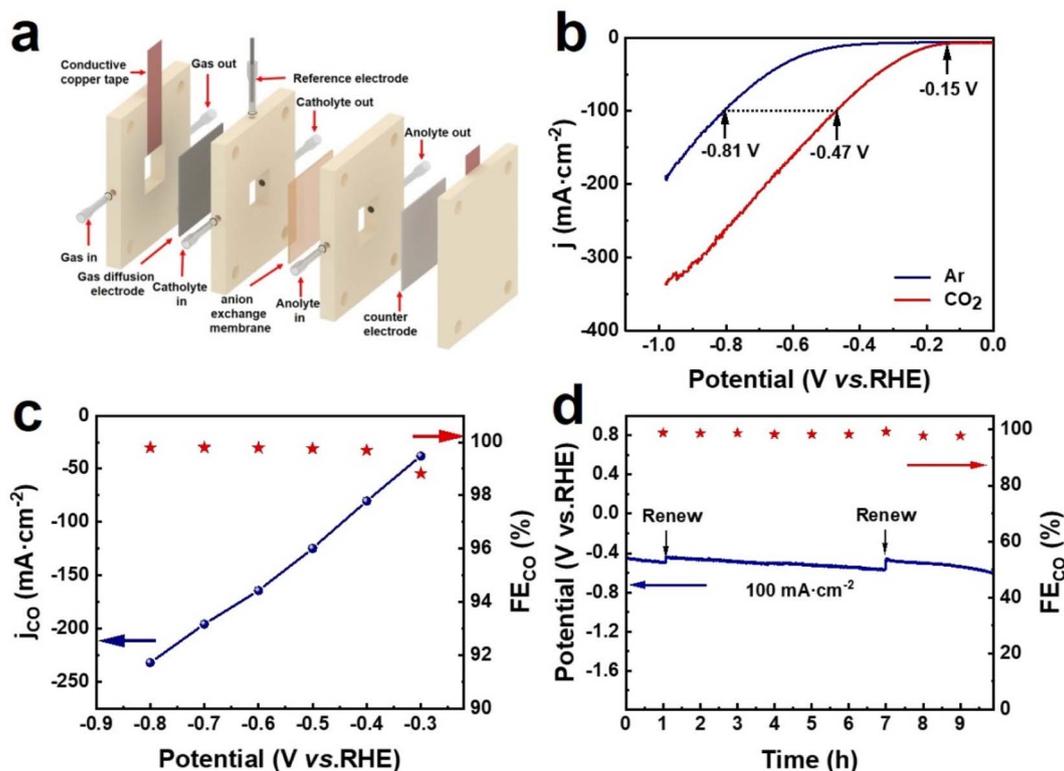
Fig. 4 (a) Schematic illustration of the flow cell electrolyzer. (b) LSV curves of the Ni-NMCF-10 catalyst under Ar or CO_2. (c) FE_{CO} and j_{CO} with different applied potentials and (d) long-term stability tests of the Ni-NMCF-10 catalyst at 100 mA cm^{-2} in the flow cell.

lowering it to 800 °C decreases j_{CO} while increasing the pyrolysis temperature to 1000 °C does not show a significant improvement in j_{CO} (Fig. S22a and b†). This may be due to the pyrolysis temperature between 800 and 1000 °C having little effect on the number of reaction sites but influencing the graphitization degree of the catalyst. Higher temperatures enhance conductivity and improve electron transport efficiency, thereby increasing the j_{CO}. Subsequently, we conducted a series of electrochemical tests to elucidate the origin of the increased activity of the Ni-NMCF-10 catalyst. Firstly, the electrochemical active surface area (ECSA) was tested by measuring the double-layer capacitance (C_{dl}) in a non-faraday region. The calculated C_{dl} values of NMCF, Ni-NMCF-10, and Ni NPs-NMC are 1.76, 3.33, and 2.71 mF cm^{-2}, respectively (Fig. 3d and S23†). The higher ECSA in the Ni-NMCF-10 catalyst indicates that it can provide more accessible reaction sites. Furthermore, the Ni-NMCF-10 catalyst delivers a Tafel slope of 146 mV dec^{-1}, much lower than that of NMCF (492 mV dec^{-1}) and Ni NPs-NMC (187 mV dec^{-1}), demonstrating that the Ni-NMCF-10 catalyst has more favorable kinetic activity (Fig. 3e). In addition, the Tafel slopes of Ni-NMCF-10 and Ni NPs-NMC catalysts are close to the value of 118 mV dec^{-1}, showing the rate-determining step (RDS) involves the transfer of the first electron to generate $CO_2^{\cdot-}$ or *COOH.[53,54] The Electrochemical Impedance Spectroscopy (EIS) test showed that, among the three catalysts, the Ni-NMCF-10 catalyst exhibited the smallest semicircle and a smaller internal resistance than that of NMCF and Ni NPs-

NMC (Fig. S24†), suggesting a more favorable charge-transfer process for CO_2 electroreduction in the Ni-NMCF-10 catalyst. In addition, a long-term eCO$_2$RR test was also carried out to evaluate the stability of the Ni-NMCF-10 catalyst. The results revealed a mild decrease in current density, with FE_{CO} remaining at approximately 99% following 12 hour electrolysis at −0.8 V (Fig. 3f), indicating its commendable durability.

2.3. Flow cell

It is known that the low solubility of CO_2 gas in electrolytes limits the current density in a typical H-type cell. However, high product selectivity and large current density (>200 mA cm^{-2}) are essential prerequisites for industrial development. Currently, the use of a gas diffusion electrode (GDE) in the eCO$_2$RR is being reported as an effective strategy to promote mass transport owing to the existence of a three-phase interface, which can realize the space separation of CO_2 gas, electrolyte and catalyst, and to avoid the low solubility of CO_2 gas in electrolytes (Fig. 4a).[55,56] Encouragingly, the Ni-NMCF-10 catalyst shows a satisfactory CO_2 reduction performance in the flow cell. The LSV curve reveals that the onset potential for the Ni-NMCF-10 catalyst is approximately −0.15 V corresponding to an overpotential of 40 mV in CO_2. In addition, the Ni-NMCF-10 catalyst can obtain a current density of 100 mA cm^{-2} at a potential of −0.47 V, which is 340 mV smaller than that under Ar (Fig. 4b). Chronopotentiometry demonstrates that the Ni-NMCF-10 catalyst exhibited a high FE_{CO} close to 100% at the range of current
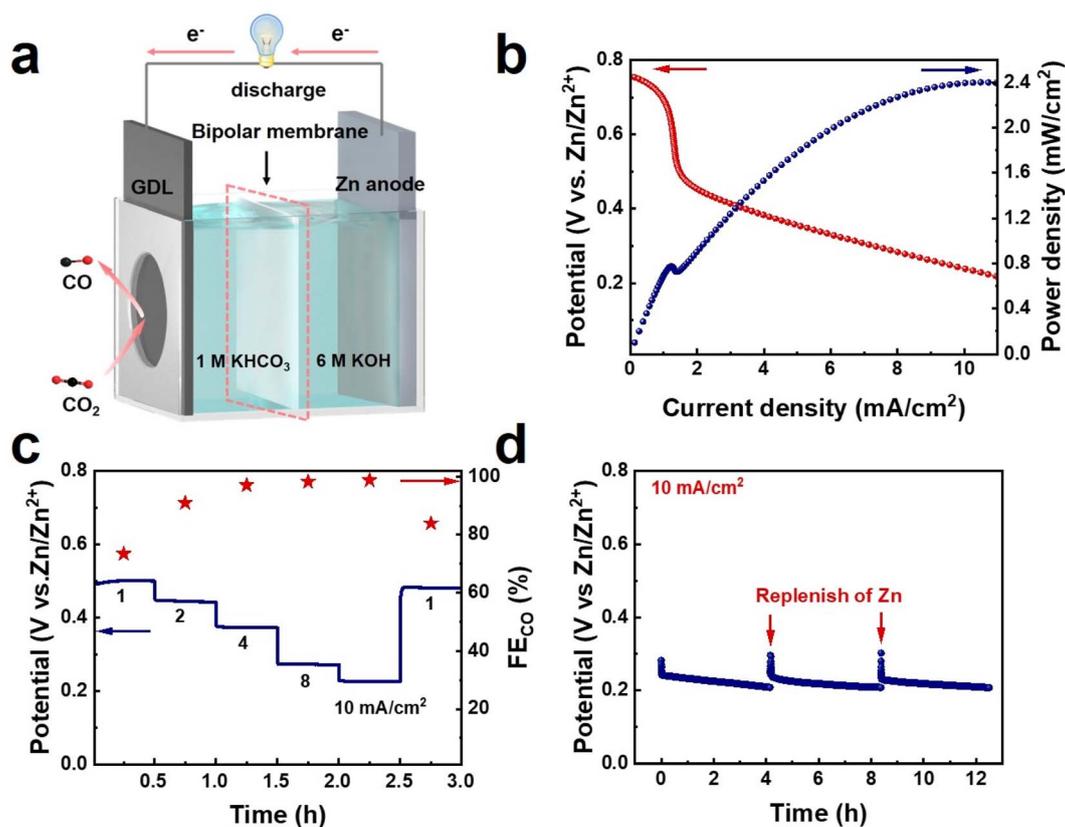
2712 | J. Mater. Chem. A, 2025, 13, 2707–2715

This journal is © The Royal Society of Chemistry 2025

Fig. 5 The application of the Ni-NMCF-10 catalyst as a cathode in an assembled Zn–CO₂ battery. (a) The configuration of the Zn–CO₂ battery; (b) polarization curves (*V–j*) and the corresponding power density curves; (c) voltage profile and corresponding FE$_{CO}$ of the Zn–CO₂ battery discharge at different current densities; and (d) long-term stability of the primary Zn–CO₂ battery with the Ni-NMCF-10 cathode at 10 mA cm^{-2}.

densities from 38 to 230 mA cm^{-2} (Fig. 4c). In addition, the Ni-NMCF-10 catalyst displays decent stability, and its current density and FE$_{CO}$ showed no obvious attenuation upon consecutive electrolysis at 100 mA cm^{-2} for 10 h (Fig. 4d).

2.4. Zn–CO₂ battery

The advancement in CO₂-based electrochemical battery systems shows significant potential in sustainable development for simultaneous high-value chemical production and electricity generation.[49,57,58] Encouraged by the superior catalytic performance of the Ni-NMCF-10 catalyst, we further assembled a novel Zn–CO₂ battery by using the Ni-NMCF-10 coated GDE as the cathode and zinc foil as the anode, respectively. A bipolar membrane was utilized to separate the cathodic and anodic electrolytes, thereby guaranteeing pH stability on either side and averting cross-contamination. It is important to note that the Zn–CO₂ battery still faces significant challenges for practical applications, such as low operating voltage, low current density, and unsatisfactory energy efficiency,[49,57] which currently do not provide clear advantages compared to the Zn–air battery that uses oxygen from the air as a reactant. Nevertheless, it holds important research value in specific applications, such as in oxygen-limited environments, including the deep sea or during Mars exploration. Moreover, when CO is produced from the CO₂RR, it is essential to consider how to effectively utilize CO as

a raw material for various chemicals, while also addressing potential safety concerns, such as CO leakage. This complexity adds to the research challenges associated with the Zn–CO₂ battery and requires considerable effort before the technology can be practically implemented. Our current work aims to further validate the high activity of the catalyst and to inspire further development of the Zn–CO₂ battery.

The schematic illustration of the Zn–CO₂ battery is presented in Fig. 5a; the dissolution of Zn occurred at the anode, while the eCO₂RR happened at the cathode during the discharge processes. The discharging polarization curve of the Ni-NMCF-10-based Zn–CO₂ battery exhibits an increased output current density with a more negative cathodic potential. It reaches a peak value of about 2.4 mW cm^{-2} (Fig. 5b), which is comparable to that of the recently reported work (Table S2†). Following discharge at current densities ranging from 1 to 10 mA cm^{-2}, the voltage plateaus decrease with a step-like pattern (Fig. 5c), and the voltage plateau almost recovers to its original value of 0.48 V (*vs.* Zn/Zn²⁺) after the current density switches back to 1 mA cm^{-2}, demonstrating good robustness of the Zn–CO₂ battery. The faradaic efficiency for CO production correlates with the current density, achieving its peak value of 98.7% at 10 mA cm^{-2}. It should be noted that the FE$_{CO}$ increased after the current density returned to 1 mA cm^{-2}. This result can be attributed to the long-term discharge process leading to

changes in the roughness of the Zn anode and the concentration of the electrolyte. Although the discharge current density of the battery returns to 1 mA cm^{-2}, the actual discharge voltage changes. Meanwhile, the applied potential in the electrolytic process has an important influence on CO selectivity. Encouragingly, we found that the Zn–CO$_2$ battery can be effectively regenerated by replenishing a new Zn plate following complete discharge without a significant voltage drop after three cycles. The battery can be continuously discharged for over 12 hours at a discharge current density of 10 mA cm^{-2} (Fig. 5d), demonstrating the long-term durability of the Ni-NMCF-10 catalyst for the eCO$_2$RR.

3. Conclusion

In summary, we report a novel self-sacrificing template-assisted wet spinning method for the rational synthesis of a 3D interconnected Ni, N-codoped macroporous carbon fiber (Ni-NCMF) catalyst. The 3D interconnected porous structure with high surface area and good electrical conductivity provides adequate accessible reaction sites and promotes electron/mass transfer dynamics. Benefitting from these advantages, the Ni-NCMF-10 catalyst exhibits outstanding CO$_2$ reduction performance with CO faradaic efficiency (FE$_{CO}$) over 95% over a wide potential window (600 mV) and achieves a maximum FE$_{CO}$ of 99.4% at -0.8 V. Furthermore, the Zn–CO$_2$ battery assembled by the Ni-NCMF-10 catalyst shows a peak power density of 2.4 mW cm^{-2} with a maximum FE$_{CO}$ of 98.7%. This work provides an alternative way to design 3D interconnected open porous nanomaterials for other electrocatalytic reactions, such as oxygen reduction, hydrogen evolution, and nitrogen reduction.

Data availability

The data and figures for this manuscript are provided in the main text and the ESI.†

Conflicts of interest

The authors declare that they have no competing financial interests or personal relationships that could have appeared to influence the work reported in this paper.

Acknowledgements

References

1 Y. Wang, Y. Liu, L. Tan, X. Lin, Y. Fang, X. F. Lu, Y. Hou, G. Zhang and S. Wang, *J. Mater. Chem. A*, 2023, **11**, 26804–26811.

2 J. Zhu, X. F. Lu, D. Luan and X. W. Lou, *Angew. Chem., Int. Ed.*, 2024, **63**, e202408846.

3 W. Zhang, Y. Hu, L. Ma, G. Zhu, Y. Wang, X. Xue, R. Chen, S. Yang and Z. Jin, *Adv. Sci.*, 2017, **5**, 1700275.

4 J. Resasco and A. T. Bell, *Trends Chem.*, 2020, **2**, 825–836.

5 Y. Zhai, P. Han, Q. Yun, Y. Ge, X. Zhang, Y. Chen and H. Zhang, *eScience*, 2022, **2**, 467–485.

6 L. Zhang, Z. J. Zhao and J. Gong, *Angew. Chem., Int. Ed.*, 2017, **56**, 11326–11353.

7 X. She, Y. Wang, H. Xu, S. Chi Edman Tsang and S. Ping Lau, *Angew. Chem., Int. Ed.*, 2022, **61**, e202211396.

8 F. Liang, K. Zhang, L. Zhang, Y. Zhang, Y. Lei and X. Sun, *Small*, 2021, **17**, 2100323.

9 M. Wang and J. Luo, *eScience*, 2023, **3**, 100155.

10 S. Jin, Z. Hao, K. Zhang, Z. Yan and J. Chen, *Angew. Chem., Int. Ed.*, 2021, **60**, 20627–20648.

11 J. Wang, Y.-C. Huang, Y. Wang, H. Deng, Y. Shi, D. Wei, M. Li, C.-L. Dong, H. Jin, S. S. Mao and S. Shen, *ACS Catal.*, 2023, **13**, 2374–2385.

12 I. A. W. Filot, R. A. van Santen and E. J. M. Hensen, *Angew. Chem., Int. Ed.*, 2014, **53**, 12746–12750.

13 Y. Yang, F. Y. Gao, X. L. Zhang, S. Qin, L. R. Zheng, Y. H. Wang, J. Liao, Q. Yang and M. R. Gao, *Angew. Chem., Int. Ed.*, 2022, **61**, e202208040.

14 P.-P. Yang and M.-R. Gao, *Chem. Soc. Rev.*, 2023, **52**, 4343–4380.

15 P. De Luna, C. Hahn, D. Higgins, S. A. Jaffer, T. F. Jaramillo and E. H. Sargent, *Science*, 2019, **364**, eaav3506.

16 X. Chen, S. Jia, C. Chen, J. Jiao, J. Zhai, T. Deng, C. Xue, H. Cheng, M. Dong, W. Xia, J. Zeng, X. Xing, H. Wu, M. He and B. Han, *Adv. Mater.*, 2023, **36**, 2310273.

17 X. Chen, S. Jia, J. Zhai, J. Jiao, M. Dong, C. Xue, T. Deng, H. Cheng, Z. Xia, C. Chen, X. Xing, J. Zeng, H. Wu, M. He and B. Han, *Nat. Commun.*, 2024, **15**, 7691.

18 S. Jia, Q. Zhu, M. Chu, S. Han, R. Feng, J. Zhai, W. Xia, M. He, H. Wu and B. Han, *Angew. Chem., Int. Ed.*, 2021, **60**, 10977–10982.

19 F. Pan, W. Deng, C. Justiniano and Y. Li, *Appl. Catal., B*, 2018, **226**, 463–472.

20 W. Ju, A. Bagger, G.-P. Hao, A. S. Varela, I. Sinev, V. Bon, B. Roldan Cuenya, S. Kaskel, J. Rossmeisl and P. Strasser, *Nat. Commun.*, 2017, **8**, 944.

21 X.-M. Hu, H. H. Hval, E. T. Bjerglund, K. J. Dalgaard, M. R. Madsen, M.-M. Pohl, E. Welter, P. Lamagni, K. B. Buhl, M. Bremholm, M. Beller, S. U. Pedersen, T. Skrydstrup and K. Daasbjerg, *ACS Catal.*, 2018, **8**, 6255–6264.

22 H. B. Yang, S.-F. Hung, S. Liu, K. Yuan, S. Miao, L. Zhang, X. Huang, H.-Y. Wang, W. Cai, R. Chen, J. Gao, X. Yang, W. Chen, Y. Huang, H. M. Chen, C. M. Li, T. Zhang and B. Liu, *Nat. Energy*, 2018, **3**, 140–147.

2714 | *J. Mater. Chem. A*, 2025, **13**, 2707–2715

This journal is © The Royal Society of Chemistry 2025

23 Y. Li, S. L. Zhang, W. Cheng, Y. Chen, D. Luan, S. Gao and X. W. Lou, *Adv. Mater.*, 2021, **34**, 2105204.

24 H. Guo, D.-H. Si, H.-J. Zhu, Q.-X. Li, Y.-B. Huang and R. Cao, *eScience*, 2022, **2**, 295–303.

25 X. Li, W. Bi, M. Chen, Y. Sun, H. Ju, W. Yan, J. Zhu, X. Wu, W. Chu, C. Wu and Y. Xie, *J. Am. Chem. Soc.*, 2017, **139**, 14889–14892.

26 K. Jiang, S. Siahrostami, T. Zheng, Y. Hu, S. Hwang, E. Stavitski, Y. Peng, J. Dynes, M. Gangisetty, D. Su, K. Attenkofer and H. Wang, *Energy Environ. Sci.*, 2018, **11**, 893–903.

27 C. Zhao, X. Dai, T. Yao, W. Chen, X. Wang, J. Wang, J. Yang, S. Wei, Y. Wu and Y. Li, *J. Am. Chem. Soc.*, 2017, **139**, 8078–8081.

28 Y. Zhang, L. Jiao, W. Yang, C. Xie and H. L. Jiang, *Angew. Chem., Int. Ed.*, 2021, **60**, 7607–7611.

29 L. Jiao, J. Zhu, Y. Zhang, W. Yang, S. Zhou, A. Li, C. Xie, X. Zheng, W. Zhou, S.-H. Yu and H.-L. Jiang, *J. Am. Chem. Soc.*, 2021, **143**, 19417–19424.

30 W. Ren, X. Tan, W. Yang, C. Jia, S. Xu, K. Wang, S. C. Smith and C. Zhao, *Angew. Chem., Int. Ed.*, 2019, **58**, 6972–6976.

31 C. Ding, C. Feng, Y. Mei, F. Liu, H. Wang, M. Dupuis and C. Li, *Appl. Catal., B*, 2020, **268**, 118391.

32 Y. Lu, H. Wang, P. Yu, Y. Yuan, R. Shahbazian-Yassar, Y. Sheng, S. Wu, W. Tu, G. Liu, M. Kraft and R. Xu, *Nano Energy*, 2020, **77**, 105158.

33 H. Wang, X. Wu, G. Liu, S. Wu and R. Xu, *Nano Res.*, 2022, **16**, 4546–4553.

34 B. Mei, C. Liu, F. Sun, S. Lu, X. Du, X. Li, F. Song, W. Xu and Z. Jiang, *ACS Catal.*, 2022, **12**, 8676–8686.

35 B. Chen, B. Li, Z. Tian, W. Liu, W. Liu, W. Sun, K. Wang, L. Chen and J. Jiang, *Adv. Energy Mater.*, 2021, **11**, 2102152.

36 D. M. Koshy, S. Chen, D. U. Lee, M. B. Stevens, A. M. Abdellah, S. M. Dull, G. C. Chen, D. Nordlund, A. Gallo, C. Hahn, D. C. Higgins, Z. Bao and T. F. Jaramillo, *Angew. Chem., Int. Ed.*, 2020, **59**, 4043–4050.

37 M. Huang, B. Deng, X. Zhao, Z. Zhang, F. Li, K. Li, Z. Cui, L. Kong, J. Lu, F. Dong, L. Zhang and P. Chen, *ACS Nano*, 2022, **16**, 2110–2119.

38 J. R. Huang, X. F. Qiu, Z. H. Zhao, H. L. Zhu, Y. C. Liu, W. Shi, P. Q. Liao and X. M. Chen, *Angew. Chem., Int. Ed.*, 2022, **61**, e202210985.

39 Y. Li, N. M. Adli, W. Shan, M. Wang, M. J. Zachman, S. Hwang, H. Tabassum, S. Karakalos, Z. Feng, G. Wang, Y. C. Li and G. Wu, *Energy Environ. Sci.*, 2022, **15**, 2108–2119.

40 Q. Hao, Q. Tang, H.-X. Zhong, J.-Z. Wang, D.-X. Liu and X.-B. Zhang, *Sci. Bull.*, 2022, **67**, 1477–1485.

41 Y. Zhang, Q. Cao, A. Meng, X. Wu, Y. Xiao, C. Su and Q. Zhang, *Adv. Mater.*, 2023, **35**, 2306831.

42 Y. S. Jun, E. Z. Lee, X. Wang, W. H. Hong, G. D. Stucky and A. Thomas, *Adv. Funct. Mater.*, 2013, **23**, 3661–3667.

43 C. Lu, J. Yang, S. Wei, S. Bi, Y. Xia, M. Chen, Y. Hou, M. Qiu, C. Yuan, Y. Su, F. Zhang, H. Liang and X. Zhuang, *Adv. Funct. Mater.*, 2019, **29**, 1806884.

44 W. Zheng, J. Yang, H. Chen, Y. Hou, Q. Wang, M. Gu, F. He, Y. Xia, Z. Xia, Z. Li, B. Yang, L. Lei, C. Yuan, Q. He, M. Qiu and X. Feng, *Adv. Funct. Mater.*, 2019, **30**, 1907658.

45 H. Yang, Q. Lin, C. Zhang, X. Yu, Z. Cheng, G. Li, Q. Hu, X. Ren, Q. Zhang, J. Liu and C. He, *Nat. Commun.*, 2020, **11**, 593.

46 S. Liang, Q. Jiang, Q. Wang and Y. Liu, *Adv. Energy Mater.*, 2021, **11**, 2101477.

47 J. Yang, Z. Qiu, C. Zhao, W. Wei, W. Chen, Z. Li, Y. Qu, J. Dong, J. Luo, Z. Li and Y. Wu, *Angew. Chem., Int. Ed.*, 2018, **57**, 14095–14100.

48 P. Lu, Y. Yang, J. Yao, M. Wang, S. Dipazir, M. Yuan, J. Zhang, X. Wang, Z. Xie and G. Zhang, *Appl. Catal., B*, 2019, **241**, 113–119.

49 F. Wang, G. Wang, P. Deng, Y. Chen, J. Li, D. Wu, Z. Wang, C. Wang, Y. Hua and X. Tian, *Small*, 2023, **19**, 2301128.

50 H. Fei, J. Dong, M. J. Arellano-Jiménez, G. Ye, N. Dong Kim, E. L. G. Samuel, Z. Peng, Z. Zhu, F. Qin, J. Bao, M. J. Yacaman, P. M. Ajayan, D. Chen and J. M. Tour, *Nat. Commun.*, 2015, **6**, 8868.

51 Y. Chen, Y. Yao, Y. Xia, K. Mao, G. Tang, Q. Wu, L. Yang, X. Wang, X. Sun and Z. Hu, *Nano Res.*, 2020, **13**, 2777–2783.

52 X. Cui, Z. Pan, L. Zhang, H. Peng and G. Zheng, *Adv. Energy Mater.*, 2017, **7**, 1701456.

53 Z. Li, Q. Zeng, Z. Ye, W. Zheng, X. Sang, C.-L. Dong, B. Yang, S. Pardiwala, J. Lu, L. Lei, G. Wu and Y. Hou, *Nano Energy*, 2021, **87**, 106187.

54 C. Kim, H. S. Jeon, T. Eom, M. S. Jee, H. Kim, C. M. Friend, B. K. Min and Y. J. Hwang, *J. Am. Chem. Soc.*, 2015, **137**, 13844–13850.

55 D. M. Weekes, D. A. Salvatore, A. Reyes, A. Huang and C. P. Berlinguette, *Acc. Chem. Res.*, 2018, **51**, 910–918.

56 W. Wang, K. Chen, Y. Sun, S. Zhou, M. Zhang and J. Yuan, *Appl. Mater. Today*, 2022, **29**, 101619.

57 J. Xie and Y. Wang, *Acc. Chem. Res.*, 2019, **52**, 1721–1729.

58 Y. Zhao, Z. Pei, X. F. Lu, D. Luan, X. Wang and X. W. Lou, *Chem Catal.*, 2022, **2**, 1480–1493.

This journal is © The Royal Society of Chemistry 2025

J. Mater. Chem. A, 2025, **13**, 2707–2715 | **2715**